A High-Speed Quadrature-Phase Rotation Shearing Interferometer for Imaging through Turbulence

B. Kern[*], P.E. Dimotakis[†], C. Martin[‡], D.B. Lang[§],
California Institute of Technology, Pasadena, California 91125
and
M. Wadsworth[¶]
California Institute of Technology / Jet Propulsion Laboratory, Pasadena, California 91109

A new technique of rotation shearing interferometry has been developed, which is optimized to reduce systematic problems when imaging through turbulence. Key improvements over previous systems are a high-frame-rate, low-noise camera and an optical system which generates four instantaneous interferograms, with instrumental phase shifts of 0°, 90°, 180°, and 270°. The simultaneous quadrature-phase interferograms enable an instantaneous complex visibility measurement in every frame. The camera system has a very short readout time, permitting high duty-cycle recording of short-exposure images, and allows tracking of individual turbulent structures as they translate across the interferograms. By eliminating sources of systematic errors and maximizing the coherence time available, astronomical measurements that far exceed what is possible using ordinary interferometric or direct-imaging techniques are attainable. Laboratory demonstrations as well as first fringes at the Palomar 200" telescope will be discussed.

I.   Introduction

The astronomical benefits of obtaining diffraction-limited imaging at visible wavelengths from ground-based 5-10 m telescopes are many. Other scientific, environmental, and military applications also await improvements in imaging through a turbulent medium, such as the atmosphere. In astronomy, a great deal can be learned about relic massive black holes, the near-nuclear environment of active galactic nuclei (AGNs), the evolution of supernova remnants, gravitational lens systems, the physics of stellar activity, and many other topics.

In order to realize the goals of diffraction-limited performance, a great deal of effort in the past three decades has gone into developing systems which overcome atmospheric limitations to resolution. Adaptive optics has been quite successful in recent years, but faces a very difficult set of problems when mi-

grating from infrared wavelengths to visible wavelengths.

A handful of rotation shearing interferometers have been used in astronomical observations,[1-4] with varying degrees of success.

II.   Interferometer Design

A.   Rotation Shearing Interferometry Concept

The new rotation shearing interferometer is a variation of a Mach-Zender interferometer configuration (see Figure 1). While a Michelson interferometer outputs just one usable interferogram (the other is sent back along the input path), in a Mach-Zender interferometer both interferograms can be used. Each interferogram in a standard Mach-Zender interferometer is an image of the input pupil, with the intensity modulated by the path-length difference between the two arms of the interferometer. Because energy is conserved, the modulation of the two interferograms is out-of-phase by 180°, i.e. where one interferogram is dark the other is light.

A rotation shearing interferometer establishes interferometric baselines by making two copies (Copy

[*]Graduate Student, Astronomy Department, Student Member AIAA
[†]Professor, Department of Aeronautics, Member AIAA
[‡]Professor, Physics Department
[§]Research Engineer, Department of Aeronautics
[¶]Principal Engineer, Space Instruments Implementation Section
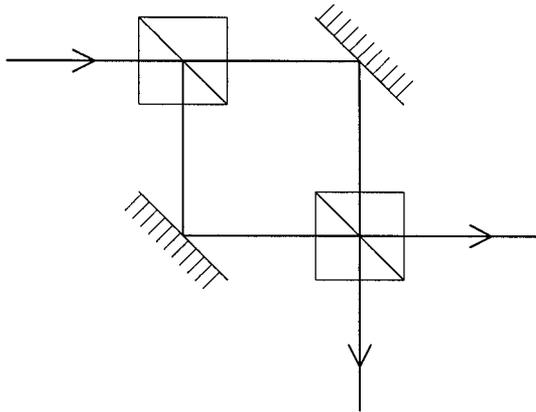
American Institute of Aeronautics and Astronautics

Figure 1: Schematic Mach-Zender interferometer arrangement, using two cube beamsplitters and two flat mirrors. Two interferograms are output.

Figure 2: Principle of rotation shearing interferometry. Copy A of the input pupil is rotated $+90°$ by Arm A, Copy B is rotated $-90°$ by Arm B. The two rotated copies of the input pupil are recombined to form two interferograms. Each point in the interferograms is a superposition of two points in the input pupil (four sample points are shown).

A and Copy B) of the input pupil, rotating those two copies by a shearing angle (180°, in this case) with respect to each other, and combining the rotated copies of the pupil (see Figure 2) to form interferograms. Arm A of the interferometer rotates Copy A by $+90°$, and Arm B of the interferometer rotates Copy B by $-90°$, so that the interferograms (Interferogram 1 and Interferogram 2) each experience a shearing angle of 180°. The intensity of any point in the interferograms is modulated by the interference between points in the input pupil separated by the shearing angle. This relationship can be generalized as

$$I_1(\vec{x}) = \langle |E(R_+(\vec{x})) + E(R_-(\vec{x}))|^2 \rangle, \qquad (1)$$

where $\vec{x} = (x, y)$ is the position vector in Interferogram 1, $R_+(\vec{x})$ is an operator which rotates the vector $\vec{x}$ by $+90°$, $R_-(\vec{x})$ is an operator which rotates the vector $\vec{x}$ by -90°, and E is the scalar electric field in the pupil. Since $R_+(\vec{x})$ and $R_-(\vec{x})$ are separated by 180°, the separation vector $(R_+(\vec{x}) - R_-(\vec{x})) = 2R_+(\vec{x})$.

The van Cittert-Zernike Theorem[5] relates the intensity modulation of points in the interferograms to the object flux distribution. The theorem states that the complex visibility function $\gamma(\vec{u})$ (also called the mutual coherence function) is the Fourier transform of the object flux distribution $F(\vec{\alpha})$,

$$\gamma(\vec{u}) = \frac{\int F(\vec{\alpha}) e^{-i(\vec{\alpha} \cdot \vec{u})} d\vec{\alpha}}{\int F(\vec{\alpha}) d\vec{\alpha}}. \qquad (2)$$

The object flux distribution F is parametrized by angle $\vec{\alpha}$, and the complex visibility function γ is
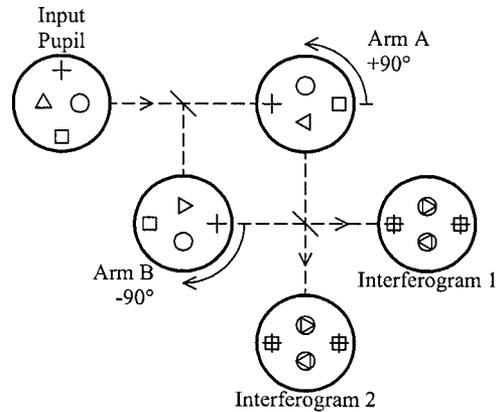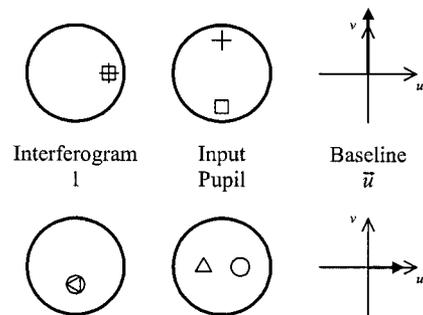

Figure 3: Two sample interferometric baselines. Points in interferogram (on left) are interferometric superpositions of points in input pupil (in center). The baselines (on right) are the vector separations between the points in the input pupil.

2
American Institute of Aeronautics and Astronautics

parametrized by the baseline vector $\vec{u} = (u, v)$ (equivalent to an angular frequency). The van Cittert-Zernike Theorem shows that the complex visibility function is measured by observing the intensity modulation resulting from interfering two points in the input pupil separated by $\Delta\vec{x}$, where

$$\vec{u} = \Delta\vec{x}\, 2\pi/\lambda \tag{3}$$
$$= (R_+(\vec{x}) - R_-(\vec{x}))\, 2\pi/\lambda \tag{4}$$
$$= R_+(\vec{x})\, 4\pi/\lambda. \tag{5}$$

A graphical example of this relationship is given in Figure 3.

In the absence of any aberrations, an optical interferometer will measure intensities according to

$$I_1(\vec{x})/\langle I \rangle = 1 + \Re\{\gamma(\vec{u})\} \tag{6}$$

where $\langle I \rangle$ is the intensity averaged over the interferogram, and $\vec{u}$ is related to $\vec{x}$ by Equation 5. Interferogram 2 differs only in the relative phase of the electric fields combined,

$$I_2(\vec{x}) = \langle |E(R_+(\vec{x})) - E(R_-(\vec{x}))|^2 \rangle, \tag{7}$$
$$I_2(\vec{x})/\langle I \rangle = 1 - \Re\{\gamma(\vec{u})\}. \tag{8}$$

The complex visibility cannot be determined from $I_1(\vec{u})$ and $I_2(\vec{u})$ alone, because I_1 and I_2 only determine $\Re\{\gamma(\vec{u})\}$. I_1 and I_2 represent measurements of the real part of the complex visibility with additive instrumental phases of 0° and 180°. In order to determine the full complex visibility, the imaginary part of $\gamma(\vec{u})$ must be measured.

B. Quadrature Phase

Because the object flux distribution $F(\vec{\alpha})$ is a real-valued function, its Fourier transform, $\gamma(\vec{u})$, is hermetian. This implies that $\Re\{\gamma(\vec{u})\} = \Re\{\gamma(-\vec{u})\}$, and so $I_1(\vec{x}) = I_1(-\vec{x})$, $I_2(\vec{x}) = I_2(-\vec{x})$, the interferograms are symmetric about the origin. This redundancy can be exploited by separating Arms A and B into upper and lower halves, which separates the interferograms into upper and lower halves. The upper halves of the arms have a zero path-length difference, and the lower halves have a $\lambda/4$ path length difference. This effectively creates four interferograms, making the interferometer a quadrature-phase interferometer.

The four interferograms, I_1^L, I_1^U, I_2^L, and I_2^U, are related by a simple phase relationship. For a given

$\vec{x}$,

$$I_1^U(\vec{x})/\langle I \rangle = 1 + \Re\{\gamma(\vec{u})\}, \tag{9}$$
$$I_1^L(-\vec{x})/\langle I \rangle = 1 + \Re\{\gamma(\vec{u})e^{i\pi/2}\}, \tag{10}$$
$$I_2^U(\vec{x})/\langle I \rangle = 1 - \Re\{\gamma(\vec{u})\}, \tag{11}$$
$$I_2^L(-\vec{x})/\langle I \rangle = 1 - \Re\{\gamma(\vec{u})e^{i\pi/2}\}. \tag{12}$$

It is mathematically convenient to deal only with the sums and differences between similar points in the interferograms,

$$\delta_U(\vec{x}) = I_1^U(\vec{x}) - I_2^U(\vec{x}), \tag{13}$$
$$\delta_L(\vec{x}) = I_1^L(-\vec{x}) - I_2^L(-\vec{x}), \tag{14}$$
$$\sigma_U(\vec{x}) = I_1^U(\vec{x}) + I_2^U(\vec{x}), \tag{15}$$
$$\sigma_L(\vec{x}) = I_1^L(-\vec{x}) + I_2^L(-\vec{x}). \tag{16}$$
$$\tag{17}$$

These variables are defined in the upper half of the interferogram space (x, y), i.e. for $y \geq 0$. $\sigma_L(\vec{x})$ should always equal $\sigma_U(\vec{x})$ to within the detector accuracy. When no aberrations are present, $\sigma_U(\vec{x}) = \sigma_L(\vec{x}) = 2\langle I \rangle$ for all $\vec{x}$.

With the complex visibility decomposed into a visiblity modulus $V(\vec{u})$ and phase $\phi(\vec{u})$,

$$\gamma(\vec{u}) = V(\vec{u})e^{i\phi(\vec{u})}, \tag{18}$$

the visibility modulus and phase are determined by

$$V(\vec{u}) = \frac{\sqrt{\delta_U^2(\vec{x}) + \delta_L^2(\vec{x})}}{(\sigma_U(\vec{x}) + \sigma_L(\vec{x}))/2}, \tag{19}$$

$$\phi(\vec{u}) = \arctan\frac{\delta_L(\vec{x})}{\delta_U(\vec{x})}. \tag{20}$$

C. Implementation

The method of splitting the interferometer into an upper and lower half is particular to the arrangement of the rotation shearing optics. The optics in each interferometer arm must rotate the pupil images by 90° and deflect the propagation vector by 90° (Figure 2). This is done using 3 mirrors in each arm (see Figure 4). In an ordinary Mach-Zender arrangement (Figure 1), the propagation vectors all lie in a plane. This nominal plane is the plane spanned by the input propagation vector and the normal to the beamsplitter diagonal.

In the new rotation shearing interferometer, the 3 mirrors in each arm deflect the propagation vectors out of this nominal plane. By deflecting the propagation vectors out of the nominal plane, the pupil images experience a net rotation. The mirrors are arranged so that this rotation, after the propagation vector is deflected out of the nominal plane

and then is deflected back into the nominal plane, is exactly 90°. The mirrors in the two arms are arranged so that they rotate the pupil images in the opposite sense, Arm A rotating Copy A of the pupil by +90°, Arm B rotating Copy B by −90°.

The third mirror in Arm B is split into an upper and a lower half. The lower half of mirror B3 is moved approximately $\lambda/8$, which gives an optical path difference of $\lambda/4$ to the rays that strike the lower half. The lower half of interferograms I_1 and I_2, I_1^L and I_2^L, have a phase difference of 90° ($\lambda/4$) relative to the upper halves, I_1^U and I_2^U.

D. Optical Design

The optics are divided into two subsystems, a direct imaging subsystem and an interferometric subsystem. The two subsystems share a common filter, chopper wheel, and focal-plane mask. Following the focal-plane mask is a beamsplitter which divides the input light between the direct imaging subsystem and the interferometric subsystem. The output of the direct imaging subsystem and the output of the interferometric subsystem are recombined in a 1:1 relay lens that conveys the in-focus image and the two interferograms onto the detector.

The direct imaging subsystem consists of a collimator, camera lens, and field lens (Figure 5). The collimator and camera lens have a combined magnification of 2. The field lens is necessary to recombine the direct image with the output of the interferometer into the relay lens.

The interferometric subsystem has just one lens (Figure 6). Assuming that the input light is telecentric (input pupil at infinity), this lens images the pupil onto the interferometer mirrors A3 and B3. A series of mirrors behind the interferometer redirect the two outputs (I_1 and I_2) so that they both pass through the relay lens to land on the same detector. Focusing the pupil image on mirror B3, which is also conjugate to the detector, ensures that the interferograms have a sharp distinction between upper and lower halves.

The outputs of both subsystems are fed through the 1:1 relay lens to land on the detector (Figure ??). The detector is conjugate to the focal-plane mask (with a magnification of 2) and to the input pupil (at infinity), which is also conjugate to mirrors A3 and B3.

E. Comparison with Other Designs

While adaptive optics has, in the last few years, succeeded in delivering excellent performance at near-
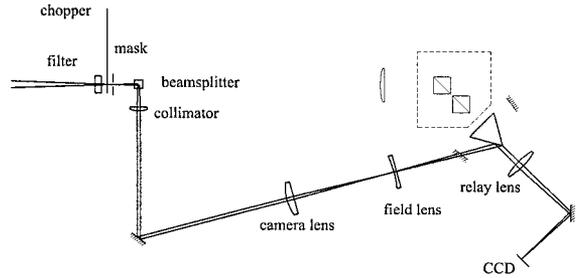
Figure 5: Direct imaging optical subsystem. Light is input from the left, focused on the focal-plane mask. The pupil is at infinity (telecentric system). The collimator and camera lens give a magnification of 2. The relay lens does not change this magnification.
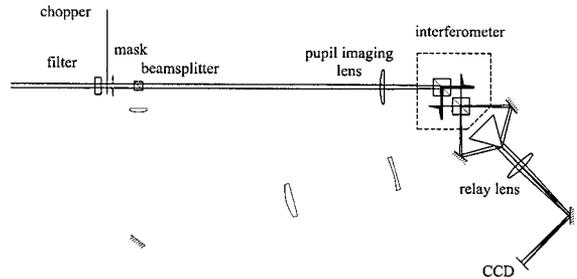
Figure 6: Interferometric optical subsystem. Light is input from the left, light rays denote marginal rays from center of pupil (pupil is at infinity). The pupil imaging lens forms an image of the pupil on the 3rd mirror in each arm of the interferometer. The relay lens relays the interferograms onto the detector.
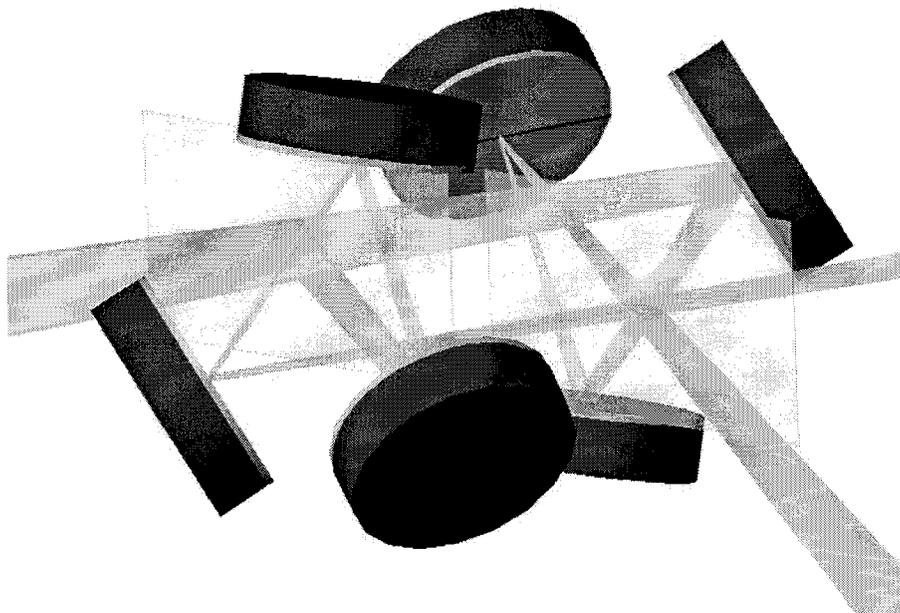
Figure 4: Mirror arrangement yielding ±90° rotation of pupil images. The two beamsplitter diagonals are shown, the three mirrors in arm A, the three mirrors in arm B, and an on-axis ray fan are shown. Arm A comprises the three mirrors on the far side of the beamsplitter diagonals, arm B comprises the three mirrors on the near side of the beamsplitter diagnoals. The third mirror in arm A (the mirror with the most visible face in this image) is split into two halves, which are displaced to give an optical path difference of $\lambda/4$. Input light (from the left side of the image) forms a pupil image on the third mirror in each arm.

infrared wavelengths, the challenges faced by adaptive optics migrating to visible wavelengths are formidable. At visible wavelengths, several passive correction approaches have been proposed or developed. These include Michelson-Fizeau interferometry, speckle imaging, non-redundant masking, and shearing interferometry. Non-redundant masking has achieved good results[6-8] and speckle interferometry has been a staple of binary star and astrometry studies for years.[9] Non-redundant masking uses only a small fraction of the light incident on the telescope, and so while large telescopes translate to higher angular resolution, the magnitude limits could be improved by using the available light sensibly. In both non-redundant masking and speckle interferometry, the Modulation Transfer Function (MTF) of the system is attenuated by the atmosphere. In order to measure true visiblity amplitudes, the instantaneous MTF must be calibrated on a reference object under the same atmospheric conditions as the observations being performed.

Shearing interferometry is a pupil-plane technique, so its MTF is essentially 100% up to the cutoff frequency D/λ. The true benefit of pupil-plane interferometry is that by ensuring that the MTF is not affected by atmospheric effects, one is not dependent on calibration of nearby objects under "identical" seeing conditions. This eliminates what is often the biggest source of systematic errors in passive correction, the atmospheric calibration.

A handful of rotation shearing interferometers have been used in astronomical observations,[1-4] with varying degrees of success. These interferometers (with the exception of the Mariotti et al.[3] interferometr) have not attempted to determine the instantaneous visibility modulus and phase. In these interferometers, the visibility modulus can be determined by measuring the variance of the intensity over time. Visibility measurements of a target must then be calibrated against a reference object under identical turbulent conditions. Since atmospheric conditions change over short timescales, this calibration technique ultimately limits the accuracy of any measurements of the visibility modulus. These simpler interferometers are unable to measure the visibility phase.

No previous astronomical shearing interferometer in the literature has obtained instantaneous phase measurements without introducing large instrumental phase gradients. The new interferometer uses "fluffed-out fringes," meaning there is no phase gradient introduced across the pupil. Introducing phase gradients severely limits fractional bandwidth and visibility modulus at high angular frequencies, and does not allow for instantaneous visibility modulus measurements. One previous shearing interferometer[3] was a phase shifting interferometer (based on a Michelson design), which varied the path length difference in the two interferometer arms over 4 exposures. By changing the path length difference by $\lambda/4$ in each exposure, the visibility phase could be determined from each set of 4 exposures. The temporal evolution of the turbulent phase variations over the 4 exposures proved to be their largest source of error. The new interferometer avoids these problems by obtaining simultaneous visibility phase and modulus measurements.

III.   Electrical Design

A.   KFS CCD Design

This interferometer must capture short-exposure images in order to freeze the turbulent variations. A new CCD system has been designed to best satisfy the interferometer's requirements of large pixel count, short readout time, and low read noise. This new CCD uses a highly parallelized design, with 32 output amplifiers, to achieve a maximum frame rate of 1000 frames per second. It is named the KFS32, short for Kilo-Frame per Second, with 32 amplifiers.

The KFS32 is a 1024 by 1036 pixel, three-phase, polysilicon-gate charge-coupled device designed for frame rates as high as 1000 frames per second. The ultra-high speed capability of the KFS32 is accomplished by segmentation and parallel operation of the CCD. As shown in Figure ??, the array contains 32 sections of 518 by 64 pixels each. Each segment consists of 512 by 64 optically-active pixels coupled to a 64 element serial register through a tapered extended parallel register that is 6 pixels by 64 pixels in size. Constructed in 50 Ωcm p-type epitaxial silicon, the 12 μm by 12 μm pixel of the imaging area can accumulate and store signals of up to 100,000 electrons.

The 32 identical segments of the CCD each contain an on-chip, three-stage, source-follower amplifier capable of supporting 40 Mpixel/sec (1000 frames per second) data rates. Amplifier stages 1 and 2 make use of on-chip current sources which function as load elements. Current levels, and hence amplifier bandwidth, can be controlled through appropriate gate bias. The use of a small FET for the input stage provides a charge-to-voltage conversion efficiency of 5.5 μV/e$^-$ at the floating diffusion sense node and an effective efficiency of 1.9 μV/e$^-$ at the output of the amplifier. An appropriately-scaled second FET provides sufficient current to drive the output FET

at high data rates. The output transistor requires an off-chip load resistor of nominally 1 kΩ value. Each amplifier requires an estimated 25 mA total bias current to function at full 200 MHz bandwidth. The total power dissipated by the 32 on-chip amplifiers is approximately 10 W.

Typically, CCD amplifiers make use of buried channel FET technology. Buried channel FETs reduce the effects of low frequency noise, such as $1/f$ noise, which is the major degradion mechanism for slow-scan CCD performance.[10] At very high bandwidths, Johnson noise is the most significant contributor to amplifier noise performance.[11] To optimize the noise performance at high data rates, all KFS32 input FETs are implemented as surface channel devices. This approach maximizes the device transconductance, thereby reducing the Johnson component of the amplifier noise. While beneficial to high frame rate operation, the use of surface channel FETs degrades the noise performance at lower data rates due to the influence of additional $1/f$ noise. Consequently, at 1 frame per second operation the measured noise floor is 12 e⁻ rms.

B. Data Acquisition System

In order to handle the large data rates that the KFS32 outputs, a set of custom A/D converters have been developed. Matching the 32 parallel output amplifiers of the KFS32 are 32 independent A/D converters, arranged in 8 VXI 4-channel A/D boards.

Each 4-channel A/D board has 4 programmable analog input stages. The gain, offset, and low-pass filter on each input channel is programmable. Each input channel also has reset clamp logic to perform Correlated Double Sampling (CDS). For a 40 MHz A/D sample rate, CDS increases the effective sampling rate to 80 MHz, but removes the per-pixel CCD reset noise. Each analog input stage feeds a 12-bit, 40 MHz A/D converter.

The digial output of each A/D converter is fed into a high-speed Digital Signal Processor (DSP), one processor per channel. The DSPs are capable of full-speed, lossless data compression with compression ratios typically ranging from 1.5 to 3.0, depending on signal level and noise. Each 4-channel A/D board has 500 MBytes of high-speed DRAM, with a board-level throughput of 320 MBytes/s, allowing full-speed recording of uncompressed data, if desired.

The on-board memory buffers can be operated in a full-speed mode where data is collected until all of the memory is full, and then the data is transferred over the VXI interface to the host computer.

Each board also has a high-speed (320 MBytes/s) auxiliary I/O port, which will allow the data to be continuously streamed to allow for real-time processing, tape storage, storage on a hard-drive array, or storage on larger external RAM buffers. The high-speed auxiliary I/O port will allow the camera to be operated at its full frame-rate for indefinite periods of time, up to the storage capacity of the external system.

IV.   Effects of Turbulence

A. Phase and Amplitude Variations

Index of refraction inhomogeneities due to turbulent mixing add phase variations to the incident wavefront. As the aberrated wavefront propagates, the phase variations will cause amplitude variations. Any interferometric imaging instrument must be able to distinguish between the phase and amplitude variations caused by propagation through the turbulent medium and the interferometric phase structure (visibility modulus and phase) due to the object flux distribution.

Previous interferometers have had difficulty separating the effects of phase and amplitude variations in interferograms. Because this interferometer captures quadrature-phase measurements, it makes independent and simultaneous measurements of the wavefront amplitude, visibility modulus, and visibility phase.

The measured visibility phase is the sum of the turbulent phase variations and the image visibility phase,

$$\phi_{\text{meas}}(\vec{u}) = \phi_{\text{image}}(\vec{u}) + \phi_{\text{turb}}(\vec{u}). \qquad (21)$$

Because the measured visibility phase is a ratio of measurements with the same amplitudes (see Equation 20), amplitude variations do not affect the measured visibility phase.

The turbulent amplitude variations are directly measured by σ_U and σ_L, which measure intensity irrespective of visibility modulus or phase. σ_U should equal σ_L, to within the detector noise. To first order, the measured visibility modulus is insensitive to amplitude variations, but amplitude variations do affect the measured visibility modulus to second order. Because the interferograms measure the superposition of two points in the input pupil, the amplitude variations from two points in the pupil are combined in the measurement of σ_U and σ_L. Given a measurement of $\sigma_U(\vec{x})$, and an estimage of the time-average of $\sigma_U(\vec{x})$ (the unaberrated intensity),

it is not possible to determine what the individual amplitude variations were at $R_+(\vec{x})$ and $R_-(\vec{x})$ independently. For instance, assume the object flux distribution is an on-axis point-source, which gives a visibility modulus $V(\vec{u}) = 1$ everywhere and a visiblity phase $\phi_{\text{image}}(\vec{u}) = 0$ everywhere. Then the scalar electric field E in the pupil is

$$E(\vec{x}) = (A_0 + \Delta A_{\text{turb}}(\vec{x}))e^{i\phi_{\text{turb}}(\vec{x})+i\omega t}, \quad (22)$$

where $\Delta A_{\text{turb}}(\vec{x})$ are the turbulent amplitude variations and $\phi_{\text{turb}}(\vec{x})$ are the turbulent phase variations. Using Equations 1, 7, 19, and 5, the measured visibility modulus is

$$V_{\text{meas}}(\vec{u}) = \frac{2(A_0 + \Delta A_+(\vec{x})))(A_0 + \Delta A_-(\vec{x})))}{(A_0 + \Delta A_+(\vec{x})))^2 + (A_0 + \Delta A_-(\vec{x})))^2}, \quad (23)$$

where $\Delta A_+(\vec{x}) = \Delta A_{\text{turb}}(R_+(\vec{x}))$ and $\Delta A_-(\vec{x}) = \Delta A_{\text{turb}}(R_-(\vec{x}))$. The effect of the amplitude variations is always a reduction in V_{meas} relative to V_{image}. If the statistics of ΔA_{turb} are known (they can be determined from a time-series of σ_U and σ_L), then the mean reduction in V_{meas} can be accounted for, but there are second-order errors that cannot be eliminated. Ignoring this issue is equivalent to assuming that $\Delta A_+(\vec{x}) = \Delta A_-(\vec{x})$.

Under typical astronomical seeing conditions, the amplitude variations should be small, even at wavelengths as short as 400 nm. However, in horizontal path propagation, or if a high-accuracy deetermination of $V(\vec{u})$ was required, the direct imaging subsystem could easily be converted into a pupil imaging subsystem, by removing the collimator and field lens. This would remove the ambiguity between ΔA_+ and ΔA_-, allowing a full correction to be made.

B. Phase Retrieval

In order to form an accurate image from the measured data, the image visibility phase ϕ_{image} must be distinguished from the turbulent phase ϕ_{turb}. The easiest way this can be done is by integration of the phasor gradients. This technique makes use of the correlation of turbulent phase variations across short distances. A Kolmogorov spectrum of phase variations gives a structure function $D_\phi(r) = 6.88(r/r_0)^{5/3}$, where $D_\phi(r)$ is the expected square of the phase difference between two points separated by $|\Delta\vec{x}| = r$. Over distances smaller than r_0, ϕ_{turb} is nearly constant.

The map of $\phi_{\text{meas}}(\vec{u})$ can be expressed as a field of phasors, of the form $e^{i\phi_{\text{meas}}(\vec{u})}$. The gradient of the phasors, $\vec{\nabla}e^{i\phi_{\text{meas}}}(\vec{u})$, contains only small turbulent phase terms. Averaging over several exposures eliminates the turbulent phase terms, leaving only

$$\langle \vec{\nabla}e^{i\phi_{\text{meas}}}(\vec{u}) \rangle = \vec{\nabla}e^{i\phi_{\text{image}}}(\vec{u}). \quad (24)$$

The gradients can be integrated to return the image phasor field, which is trivially converted into the image visibility phase.

The method of integration of phasor gradients does not depend on the statistics of the phase variations. As long as the structure function $D_\phi(\Delta\vec{x})$ is small for some $\Delta\vec{x}$ (and zero for $\Delta\vec{x} = 0$), the method of integration of phasor gradients will yield the image visibility phase.

C. Wavefront prediction

A time-series record of the measured phase ϕ_{meas} can be used to improve the measurement accuracy of both the turbulent phase variations and the image visibility phase. The turbulent phase variations have some characteristic timescale over which they evolve, measured in the moving frame of the atmosphere (carried by the bulk wind velocity). Studies have shown that in astronomical observing conditions, this timescale is in the range of 0.3 s.[12] This characteristic timescale defines a maximum exposure time τ_{max} if the phase variations were observed in a reference frame comoving with the bulk wind.

The exposure times needed to freeze the turbulent phase variations are usually determined by some bulk wind speed, often in the range of ~ 10 m/s. The time in which turbulent phase variations with a size scale of ~ 10 cm travelling at 10 m/s become blurred is $\tau_{\text{blur}} \sim 10$ ms. Since the turbulent phase variations are not actually changing on this timescale, the same turbulent structures are simply translated across the input pupil by the bulk wind speed between successive exposures. By examing a series of successive exposures, the coherent turbulent structures can be tracked as they are translated across the input pupil. The measurements of the turbulent phase variations taken from a series of exposures can be coherently added by applying the correct translations between exposures. The improvement in the accuracy of the measurement of the phase variations is then equivalent to increasing the exposure time from τ_{blur} to τ_{max}, an increase by a factor of ~ 30.

Adaptive optics systems have hoped to apply this concept to wavefront sensor data, with some preliminary success.[13] The advantage of performing this analysis offline is that the information from both past and future times can be used to improve the

measurement of an individual turbulent phase variation.

The improvement in measurement precision realized by using all of the available $\tau_{\max}$ can be quite substantial. An improvement in the effective exposure time available by a factor of 30 means that the number of objects that can be studied (as limited by the brightness of those objects) increases by $30^{3/4}$, assuming the objects are distributed uniformly in space.

V.   Results

¡Palomar results¿ Brian
    ¡Future lab results¿ Brian

VI.   Future Applications

To achieve short-term astronomical goals, this rotation shearing interferometry (RSI) will be used in a differential mode.[14] This mode allows measurement of relative spatial offsets of different spectral components, to a level of precision well beyond the diffraction limit of the telescope. Using this technique on the broad-line emission regions of nearby Seyfert Is (i.e. NGC 3227, NGC 4051, possibly PG 1226+023), spatial offsets of < 100 μarcsec can be measured between the red and blue wings of broad lines. This is smaller than the radius of the broad-line region predicted from reverberation mapping.[15,16] This would allow the first direct determination of the size and structure of the broad-line regions – whether the broad lines obey an ordered rotation or if the red- and blue-shifted components have no spatial separation.

References

[1] J.B. Breckinridge. A two-dimensional white-light amplitude interferometer. In J. Davis and W. Tango, editors, *High Angular Resolution Stellar Interferometry*, pages 31–1 – 31–13. Chatterton Astron. Dept., 1979.

[2] C. Roddier and F. Roddier. High angular resolution observations of Alpha Orionis with a rotation shearing interferometer. *Astrophys. J.*, 270:L23–26, 1983.

[3] J.M. Mariotti, J.L. Monin, P. Ghez, C. Perrier, and A. Zadrozny. Pupil plan interferometry in the near infrared I. Methodology of observation and first results. *Astron. Astrophys.*, 255:462–476, 1992.

[4] C.M. de Vos, J.D. Bregman, and U.J. Schwarz. Pupil plane interferometry: Some conclusions from SCASIS. In J.G. Robertson and W.J. Tango, editors, *Very High Angular Resolution Imaging*, pages 419–420. Kluwer, 1994.

[5] A. Richard Thompson, James M. Moran, and George W. Swenson Jr. *Interferometry and Synthesis in Radio Astronomy*. Wiley, 1986.

[6] J.E. Baldwin, C.A. Haniff, C.D. Mackay, and P.J. Warner. Closure phase in high-resolution imaging. *Nature*, 320:595–597, 1986.

[7] A.C.S. Readhead, T.S. Nakajima, T.J. Pearson, G. Neugebauer, J.B. Oke, and W.L.W. Sargent. Diffraction-limited imaging with ground-based optical telescopes. *Astron. J.*, 95:1278–1296, 1988.

[8] P.G. Tuthill, C.A. Haniff, and J.E. Baldwin. Surface imaging of long-period variable stars. *Monthly Not. R. Astron. Soc.*, 306:353–360, 1999.

[9] A.M. Ghez, B.L. Klein, M. Morris, and E.E. Becklin. High proper-motion stars in the vicinity of Sagittarius A* Evidence for a supermassive black hole at the center of our galaxy. *Astrophys. J.*, 509:678–686, 1998.

[10] R.W. Broderson and S.P. Emmons. Noise in buried channel charge-coupled devices. *IEEE J. Solid State Circuits*, SC-11:147–155, 1976.

[11] M.H. White, D.R. Lampe, F.C. Blaha, and I.A. Mack. Characterization of surface channel CCD image arrays at low light levels. *IEEE J. Solid State Circuits*, SC-9:1–13, 1974.

[12] B. Kern, T.A. Laurence, C. Martin, and P.E. Dimotakis. Temporal coherence of individual turbulent patterns in atmospheric seeing. *Appl. Opt.*, 39:4879–4885, 2000.

[13] C. Dessenne, P.-Y. Madec, and G. Rousset. Sky implementation of modal predictive control in adaptive optics. *Opt. Lett.*, 24:339–341, 1999.

[14] J.M. Beckers. "Differential speckle interferometry," a new tool for double star research. In R.S. Harrington and O.G. Franz, editors, *Current Techniques in Double and Multiple Star Research*, pages 165–175. Lowell Observatory, 1981.

[15] A. Wandel, B.M. Peterson, and M.A. Malkan. Central masses and broad-line region sizes of active galactic nuclei. I. Comparing the photoionization and reverberation techniques. *Astrophys. J.*, 426:579–591, 1999.

[16] S. Kaspi, P.S. Smith, H. Netzer, D. Maoz, B.T. Jannizu, and U. Giveon. Reverberation measurements for 17 quasars and the size-mass-luminosity relations in active galactic nuclei. *Astrophys. J.*, 533:631–649, 2000.